

Spin-polarized correlated insulator in monolayer MoTe_{2-x}

Zemin Pan^{1#}, Wenqi Xiong^{1#}, Jiaqi Dai^{2,3#}, Yunhua Wang⁴, Tao Jian¹, Xingxia Cui¹, Jinghao Deng¹, Xiaoyu Lin¹, Zhengbo Cheng¹, Yusong Bai¹, Chao Zhu¹, Da Huo¹, Geng Li^{5,6}, Min Feng¹, Jun He^{1,7}, Wei Ji^{2,3*}, Shengjun Yuan^{1,7*}, Fengcheng Wu^{1,7*}, Chendong Zhang^{1,7*}, and Hong-Jun Gao⁵

¹*School of Physics and Technology, Wuhan University, Wuhan 430072, China*

²*Beijing Key Laboratory of Optoelectronic Functional Materials & Micro-nano Devices, Department of Physics, Renmin University of China, Beijing 100872, China*

³*Key Laboratory of Quantum State Construction and Manipulation (Ministry of Education), Renmin University of China, Beijing, 100872, China*

⁴*Key Laboratory of Quantum Theory and Applications of Ministry of Education and School of Physical Science and Technology, Lanzhou University, Lanzhou 730000, China*

⁵*Beijing National Center for Condensed Matter Physics and Institute of Physics, Chinese Academy of Sciences, Beijing 100190, China*

⁶*Hefei National Laboratory, Hefei 230088, China*

⁷*Wuhan Institute of Quantum Technology, Wuhan 430206, China*

**Correspondence and request for materials should be addressed to:*

wji@ruc.edu.cn (W.J.), s.yuan@whu.edu.cn (S.J.Y.), wufcheng@whu.edu.cn (F.C.W.),
cdzhang@whu.edu.cn (C.D.Z)

Abstract: Flat electronic bands near the Fermi level provide a fertile playground for realizing interaction-driven correlated physics. To date, related experiments have mostly been limited to engineered multilayer systems (*e.g.*, moiré systems). Herein, we report an experimental realization of nearly flat bands across the Fermi level in monolayer MoTe_{2-x} by fabricating a uniformly ordered mirror-twin boundary superlattice (corresponding to a stoichiometry of $\text{MoTe}_{56/33}$). The kagome flat bands are discovered by combining scanning tunnelling microscopy and theoretical calculations. The partial filling nature of flat bands yields a correlated insulating state exhibiting a hard gap as large as 15 meV. Moreover, we observe pronounced responses of the correlated states to magnetic fields, providing evidence for a spin-polarized ground state. Our work introduces a monolayer platform that manifests strong correlation effects arising from flattened electronic bands.

Suppressing electron kinetic energy in solids through the creation of less dispersive flat bands (FBs) is a promising route to enhance many-body correlation effects¹. In addition to mundane cases attributed to atomic orbital localizations [*i.e.*, flat atomic bands (FABs)], wavefunction overlapping and electron hopping processes are preserved in flat topological bands (FTBs), where the suppression of kinetic energy arises from destructive interference effects^{2,3}. Examples of FTBs are obtained in artificially engineered van der Waals systems by creating moiré supercells that fold and flatten the band structure⁴⁻⁸. In twisted bilayer graphene (TBG), the flat bands are near the E_F (Fermi energy), leading to correlated insulating states⁸⁻¹⁰, magnetism^{10,11}, and strong-coupling superconductivity^{12,13} tuned by twist angle and electron doping. However, due to the large size of the moiré supercell in real space, the carrier densities in those moiré samples are usually low². In addition, the existence of flat bands (FBs) and the corresponding quantum phases in TBG have strict stacking-angle requirements⁵, posing challenges to attain practical samples at the meso/macro scale, which is essential for technological applications.

Although some of the limitations might be overcome in natural crystalline materials, the FTB has yet to be realized in stoichiometric materials with high quality. Recent theoretical efforts have addressed this issue by predicting a large library of candidates (*e.g.*, $\text{KAg}(\text{CN})_2$, and $\text{Pb}_2\text{Sb}_2\text{O}_7$) via high-throughput calculations². Experimentally, extensive research has been performed on transition metal kagome magnets¹⁴⁻¹⁹, such as Fe_3Sn_2 , $\text{Co}_3\text{Sn}_2\text{S}_2$, and YMn_6Sn_6 , where the transition metal atoms form a corner-shared triangle network. Due to the nonnegligible hopping along the z -direction, the flat

bands in these 3D compounds usually occupy a limited momentum space and/or are not isolated in the energy space¹⁸⁻²⁰. In this sense, single atomically thin crystals should be a preferable platform to manifest 2D kagome physics in a neat way. A colouring-triangular lattice has recently been visualized in a Mo_5Te_8 monolayer, in which two sets of kagome bands are found locating away from the Fermi level by tens of meV²¹. Thus, the correlated phenomena driven by the FBs right at the E_F have yet to be realized in the single-atomic-layer limit.

In this work, we show that by well-controlled postgrowth annealing, telluride atoms in monolayer H-MoTe₂ desorb, transforming the monolayer into a distinct phase ($\text{MoTe}_{56/33}$) exhibiting a lattice constant of 19.1 Å. The $\text{MoTe}_{56/33}$ monolayer contains an ultradense, uniformly sized mirror twin boundary (MTB) superlattice, which is thermally favourable under a certain range of Te chemical potentials. We emphasize that the MTBs form a periodic lattice rather than the previously identified local line defects with metallic defect states²²⁻²⁴ or harbouring 1D correlation phenomena, such as 1D charge density waves (CDWs) or Luttinger liquids²³⁻²⁶. By combining scanning tunnelling microscopy (STM), noncontact atomic force microscopy (nc-AFM), and theoretical calculations, we reveal that the formation of an MTB supercell results in FTBs residing inside the pristine band gap of H-MoTe₂. Two sets of kagome bands are mixed across the E_F , which results in partially filled bands sitting at the Fermi level, where a hard gap of 15 meV was experimentally measured at 0.35 K. This gap was elucidated to be a correlated one by temperature-dependent spectroscopic measurements. In addition, magnetization-polarized Zeeman shifts are observed for the

occupied and unoccupied bands, suggesting that the correlated insulating states are spin polarized. This work demonstrates a new route for materializing exotic FB-driven quantum phases in a vdW monolayer via easy and scalable structural engineering.

H-phase monolayer MoTe₂ was synthesized on bilayer graphene (BLG)/SiC (0001) by utilizing a delicate MBE method [see Methods]. We obtained an ordered superstructure phase dominating the monolayer sample prepared at annealing temperatures ($T_{\text{annealing}} = 450$ °C after postgrowth annealing from the H phase. The zoomed-in images of this superstructure (Fig. 1b) show the apparent wagon-wheel morphology, which is composed of six lines (spokes of the wagon-wheel) encircled in a skewed hexagonal pattern. The periodicity of this superlattice is 1.91 nm. The line boundaries appear as bright stripes at high sample bias (2.0 V in Fig. 1b), and they manifest as dark trenches at low sample bias (0.8 V in Fig. 1c). These morphologic characteristics resemble the STM results of the MTBs formed in other H-phase TMDs^{27,28}. An argument was raised in recent work that this 1.91 nm superperiodicity in MoTe₂ could be a moiré pattern²⁹. In Fig. S1, we show that its appearance is independent of the twist angle relative to the BLG substrate, and it could also be prepared on a WSe₂ substrate, thus ruling out the possibility of a moiré pattern.

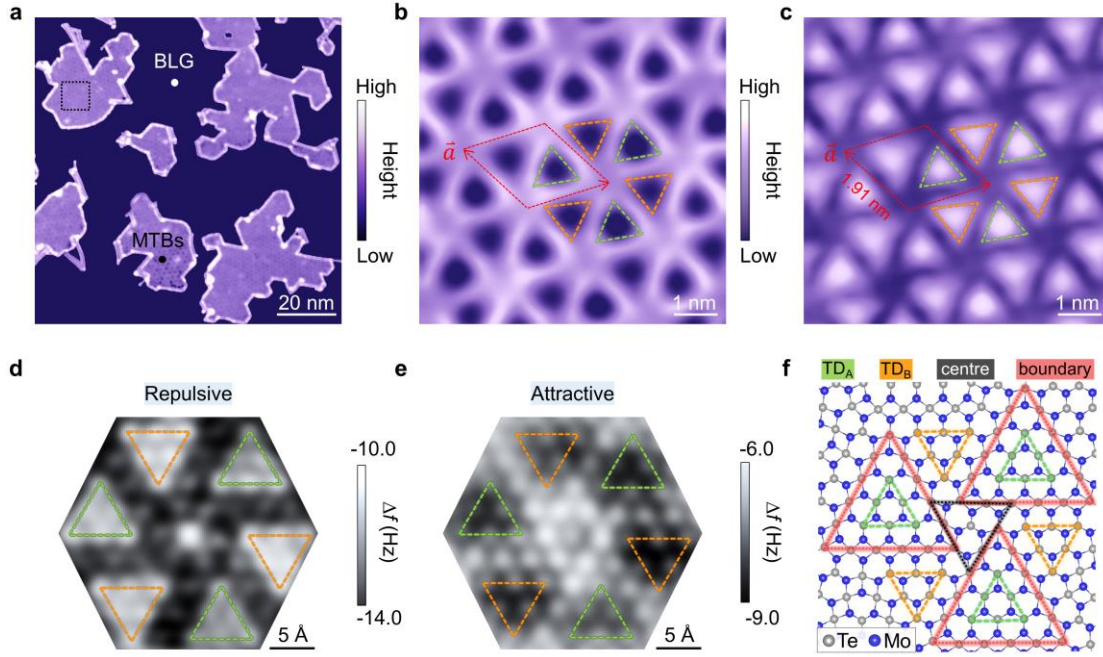


Fig. 1 | Fabrication of the MTB superlattice and its atomic structure. **a**, Large-scale STM topographic image of the sample hosting the dominant portion of the MTB superlattice. **b**, **c**, Zoomed-in STM images of the marked region in **(a)** showing the apparent wagon-wheel pattern. The supercell is labelled a red rhombus with a lattice constant of 1.91 nm. **d**, **e**, Atomically resolved nc-AFM images acquired in the repulsive and attractive regimes, respectively (details in Fig. S2). Only the top-layer Te atoms are shown. **f**, Atomic model of the MTB superlattice. Grey and blue balls represent Te and Mo atoms, respectively. The boundary-formed triangular loops (MTB loops), TD_A, TD_B, and centre sites are marked as shown. Scanning parameters: **(a)** bias voltage $V_{\text{bias}} = 1$ V, tunnelling current $I_t = 10$ pA, **(b)** 2 V, 50 pA, **(c)** 0.8 V, 50 pA.

Frequency-shift nc-AFM images (Figs. 1d and 1e) offer further information on the atomic structures. According to previous nc-AFM studies of the MTBs^{26,30} in TMDs, only the top-layer Te atoms are imaged here. There are discernible and reversible (in the repulsive and attractive force regimes) contrasts in the Te atoms between the boundary and the domain regions, which can be attributed to the discrepancy of their relative heights and/or electron densities^{26,30}. Each triangular domain consists of six top-layer Te atoms (*i.e.*, three Mo-Te units) with an interatomic distance of 0.365 nm, nearly the same as that in pristine H-MoTe₂. In both images, there is one Te atom at the rotational centre. Based on these observations, we propose an atomic structure for the

observed superlattice, as schematically shown in Fig. 1f³¹. The validity of this model was further verified by its lowest formation energy among various candidate models in a certain range of the Te chemical potential (Fig. S3) and the agreements between experiment-theory comparisons of bias-dependent dI/dV images (Fig. S4). Te atoms on the MTB form closed triangular loops, which were previously termed MTB loops³². We denoted the MoTe₂ domain enclosed by individual MTB loops as domain A (TD_A), while domain B (TD_B) is located among three MTB loops. The corner joint region of three MTB loops is denoted as the centre site. Given this detailed atomic model, we revealed the Mo:Te ratio of this phase to be 33:56; therefore, the rigorous stoichiometry is MoTe_{2-x} with $x = 10/33$.

Although the notion of an MTB network has been previously reported, we emphasize that the present structure is distinctive in two aspects: the smallness and uniformity of the 1.91-nm periodicity over the whole monolayer sample. Therefore, a periodic potential should modify the electronic behaviour globally rather than the previously used local defect picture^{23,27}. Figure 2a plots the differential conductance spectra (dI/dV) of both MoTe_{56/33} and H-MoTe₂ monolayers for a clearer comparison. Inside the approximately 2 eV band gap of H-MoTe₂²⁹, at least five pronounced peaks were observed in the MoTe_{56/33} spectrum, labelled P₋₁, P₀, P₁, P₂, and P₃ in ascending order of energy. Among these peaks, P₀ resides across the Fermi level along with a zero-bias dip feature. Moreover, the spatially dependent dI/dV spectra of four representative sites (Fig. 2b) indicate that the zero-bias dip feature of P₀ presents, with varying weights, over major regions of the supercell. This result confirms that the observed peaks should

be viewed as a property of the system as a whole instead of localized defect states. In Fig. S5, we thoroughly inspect the transition of local boundary states into delocalized states as the interboundary separation shrinks.

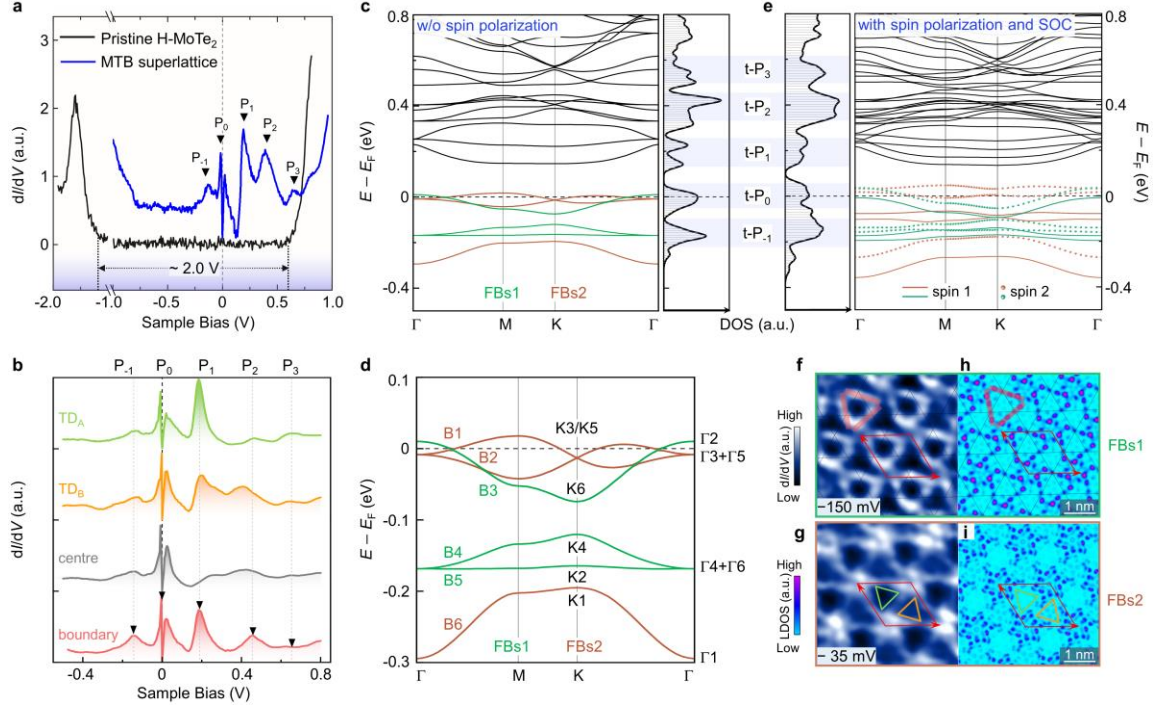


Fig. 2 | Emergence of flat bands near the Fermi level. **a**, Experimental dI/dV spectra acquired on pristine H-MoTe₂ (black line) and a typical spectrum of the MTB superlattice (blue line). **b**, Experimental dI/dV spectra taken at four high-symmetry sites (TD_{A/B}, centre, and boundary). **a**, **b**, Five pronounced sharp peaks are labelled P₋₁, P₀, P₁, P₂, and P₃. **c**, Calculated band structures of the MTB supercell without spin polarization plotted along high-symmetry momentum paths in the Brillouin zone. The spin-polarized calculation with SOC included is displayed in **e**. The plots of DOS are shown in the side panel. The five regions with intensity maxima are marked as t-P₋₁ to t-P₃. **d**, Zoomed-in plot of **c** on the six bands near the Fermi level (-0.3 eV to 0.1 eV). The irreps of states at Γ and K momenta are labelled for each band (Table S1). The green and brown lines mark states that are odd (FBs1) and even (FBs2), respectively, under mirror operation \hat{M} . **f**, **g**, Measured dI/dV maps at energies of -150 mV and -35 mV, respectively. Calculated LDOS maps at “ $\Gamma 4 + \Gamma 6$ ” (FBs1) and “K3 + K5” (FBs2) are displayed in **(h, i)**. The black lines in **(f, h)** serve as a visual guide, illustrating the kagome pattern. The boundary region is depicted by the red shadows in **(f, h)**. The green and orange triangles in **(g, i)** represent the TD_A and TD_B regions, respectively. The red rhombus indicates a supercell. The stabilization parameters in **(a)** are $V_{\text{bias}} = 1.0$ V, $I_t = 100$ pA, and lock-in modulation $V_{\text{mod}} = 8$ mV; in **(b)** are $V_{\text{bias}} = 0.8$ V, $I_t = 200$ pA, and lock-in modulation $V_{\text{mod}} = 4$ mV; and in **(f, g)** are $I_t = 200$ pA and $V_{\text{mod}} = 1$ mV.

Figures 2c and 2e plot the density-functional theory (DFT) band structures in which the spin degree of freedom was non-polarized and polarized (with consideration of spin-

orbit coupling, SOC), respectively. An on-site Coulomb potential $U = 0.5$ eV was used in all calculations, and the U dependence on electronic structures is discussed in Fig. S7. Notably, although the band/spin degeneracies are lifted in the spin-polarized band structure in tens of meV, both the spin-nonpolarized and spin-polarized band structures show comparable overall line shapes of their associated density of states (DOS), as shown in Figs. 2c and 2e. In particular, they both primarily resemble the spectroscopic peaks P₋₁ to P₃, with one peak located right at the E_F . The zero-bias dip on P₀ is absent in both DFT DOSs, indicating a likely strong correlation nature, which we discuss later.

These DOS maxima correspond to a cascade of nearly dispersion-free bands (namely, FBs), as presented in the band structure. For simplification, we use the spin-nonpolarized band structure (Fig. 2c) to discuss the origin of these nearly flat bands. Near the Fermi level (-0.3 eV to $+0.1$ eV), there are six bands with a relatively simple structure. In a close-up panel on this energy window (Fig. 2d), we label them B1–B6 in descending order of energy. B1–B3 overlap in energy around the Fermi level, which corresponds to the P₀ states. B4–B6 are located at slightly lower energy levels and correspond to the P₋₁ states. Our subsequent discussions are mainly focused on these six bands near the Fermi level, while a brief discussion for P₁–P₃ is provided in Fig. S5.

We next unravel the origin of the dispersionless B1–B6 bands as kagome flat bands based on the symmetry analysis. The MTB lattice has the space group $P\bar{6}$ (No. 174) and the C_{3h} point group, which includes a threefold rotation \hat{C}_{3z} around the out-of-plane \hat{z} axis and a mirror symmetry \hat{M} by the xy plane. The six bands of B1–B6 can be classified into two groups that are odd (B3, B4, B5, as FBs1) and even (B1, B2, B6, as

FBs2) under the \widehat{M} operation (details in Supplementary Table S1), as marked by the green and brown lines in Fig. 2d, respectively. In the mirror odd sector, bands B3, B4, and B5 have the prototypical energy dispersion of a kagome lattice without inversion symmetry. The B5 band is nearly flat and touches the B4 band at the Γ point (Brillouin zone centre), and the B3 and B4 bands are separated by an energy gap at the K point (Brillouin zone corner). The formation of an effective kagome lattice by these three bands can be established theoretically using band representation theory³³. The irreducible representations (irreps) of the three bands are calculated to be $\Gamma_2 + \Gamma_4 + \Gamma_6$ and $K_2 + K_4 + K_6$ at Γ and K points, respectively (Fig. 2d). These symmetry data are the same as those for bands formed by Wannier orbitals placed at the $3j$ Wyckoff positions, *i.e.*, three inequivalent sites per unit cell that are related by threefold rotation³⁴. From geometry, the $3j$ Wyckoff positions indeed form an effective kagome lattice.

Moreover, the effective kagome lattice can also be revealed by the real-space distribution. Notably, the three bands within one set of FBs have similar wavefunctions (Fig. S7); here, we take the $\Gamma_4 + \Gamma_6$ states from the B4 and B5 bands as an example (Fig. 2h), where the local density of states (LDOS) peaks along the MTBs. The calculated result closely matches the experimental conductance mapping for the P_{-1} state (Fig. 2f). The centres of the boundaries form a breathing kagome lattice (illustrated by the grid in Figs. 2f and 2h) that is akin to the line graph of a honeycomb lattice³⁵. Based on similar analysis, FBs2 can also be attributed to kagome bands and have good consistency with experimental mapping for the P_0 state, as shown in Figs. 2g and 2i.

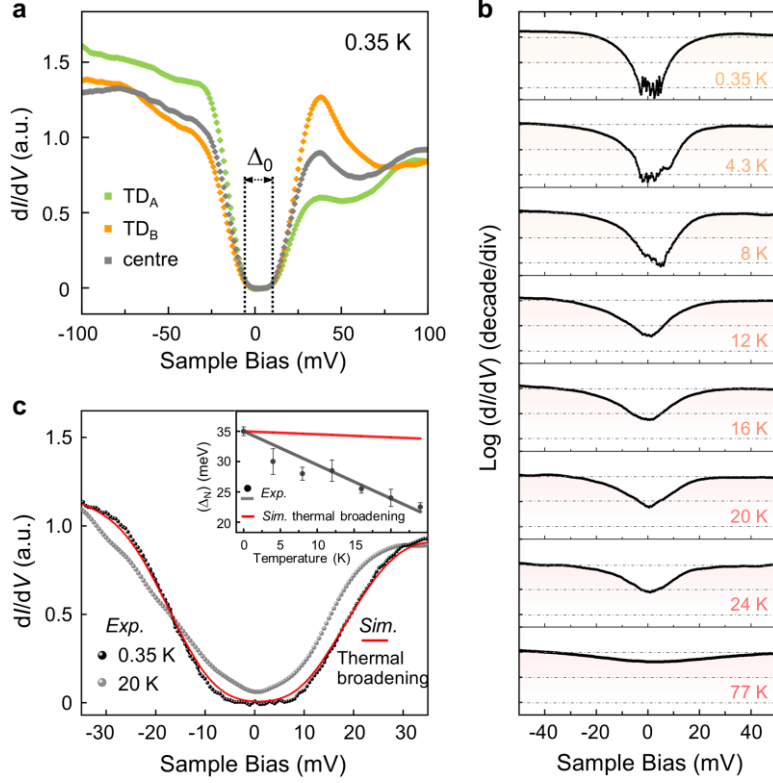


Fig. 3 | Experimental evidence for the correlated insulator. **a**, High-resolution dI/dV spectra recorded at the $TD_{A/B}$ and centre sites at $T_{\text{sample}} = 0.35$ K, showing a hard energy gap with a relatively uniform magnitude. Δ_0 denotes the size of the zero-conductance region, and Δ_N is the gap defined by the midpoints of the edge slopes, *i.e.*, the maximum point in the $|d^2I/dV^2|$ spectra (see Fig. 4 for details). **b**, Temperature-dependent dI/dV spectra near the energy gap (centre site) ranging from 0.35 K–77 K. The spectra lines are plotted on a logarithmic scale. **c**, Selective spectra taken at 0.35 K (black curve) and 20 K (grey curve). The red curve corresponds to a simulation by applying thermal broadening (with $T = 20$ K) to the black curve. The inset shows the experimental Δ_N (black circles) values at different T_{sample} values with a visual guide (grey line). The red line is the simulated $\Delta_N(T)$, which is found by applying thermal broadening to the 0.35 K spectrum. Stabilization parameters: $V_{\text{bias}} = 100$ mV, $I_t = 200$ pA, and $V_{\text{mod}} = 2$ mV.

Next, we discuss the puzzling dip at the Fermi level. In Fig. 3a, we present high-resolution tunnelling spectroscopy within a zoomed-in energy range (± 100 meV) taken at 0.35 K. A hard gap can be determined unambiguously with $\Delta_0 \sim 15$ meV for the zero-conductance region. The magnitude of Δ_0 persists among different locations, although minor differences in the line shapes occur. To determine the origin of this hard gap, we measured its evolution with temperature. As shown in Fig. 3b, the hard gap continuously narrows with increasing temperature and closes above 12 K. However,

the observed gap closing cannot be explained only by thermal broadening. In Fig. 3c, we take the lowest-temperature spectrum (*i.e.*, 0.35 K, black curve) to simulate the thermal broadening with $T = 20$ K (red curve, see Supplementary Note 1), which deviates significantly from the measured curve at 20 K (grey curve). To quantify the gap size over a wide temperature range, we define Δ_N by the midpoints of the edge slopes. The inset shows the simulated thermal broadening of Δ_N and the experimentally measured values as a function of temperature, where the experimental results exhibit a rapid decay. This spectroscopic behaviour demonstrates the correlated nature of the observed gap^{36,37} rather than the single-particle gap observed in the cousin system of monolayer Mo_5Te_8 ²¹.

Regarding the mechanism of gap formation, the CDW gap and the quantum confinement effect can first be ruled out by supplementary experimental results, in which no charge modulations was seen in the bias-dependent STM imaging (Fig. S8), and the gap size is independent of the monolayer flake size (Fig. S9). The possibility of the superconducting gap is also excluded as the gap cannot be suppressed by applying magnetic fields. However, other responses of the insulating states to the magnetic field appear surprisingly. Figure 4a shows the dI/dV spectra of the correlation gap taken under magnetic fields applied perpendicularly to the sample basal plane (*i.e.*, z direction). The unoccupied and occupied edges both shift progressively towards lower energies with increasing field magnitude independent of the $+z$ or $-z$ field direction. For quantitative analysis, we take the peak positions in the second derivative spectra (Fig. 4b) to represent the energy locations of gap edges. The energy shifts ΔE for both

unoccupied and occupied edges exhibit a linear relationship with the magnitude of \mathbf{B} , conforming to the Zeeman-type energy shift. The sign of ΔE regardless of the field direction can be understood as a magnetization-polarized Zeeman effect^{16,17}, which indicates the following facts: net magnetic moments exist (at least locally) in the MoTe_{56/33} monolayer and the moments \mathbf{m} are always parallelly aligned to the external field direction (in our measurements, a nonzero minimum $|\mathbf{B}|$ is 2 T). The values of the effective magnetic moment (m_{eff}) can be extracted from the linear fitting of the Zeeman shift $\Delta E = -\mathbf{m}_{eff} \cdot \mathbf{B}$ (as labelled in Figs. 4c and 4d)^{16,17}. With statistical analyses of multiple measurements over the superlattice (Figs. 4e and 4f), we determined m_{eff} to be $0.4 \pm 0.3 \mu_B$ and $3.0 \pm 0.3 \mu_B$ for the unoccupied and occupied states, respectively.

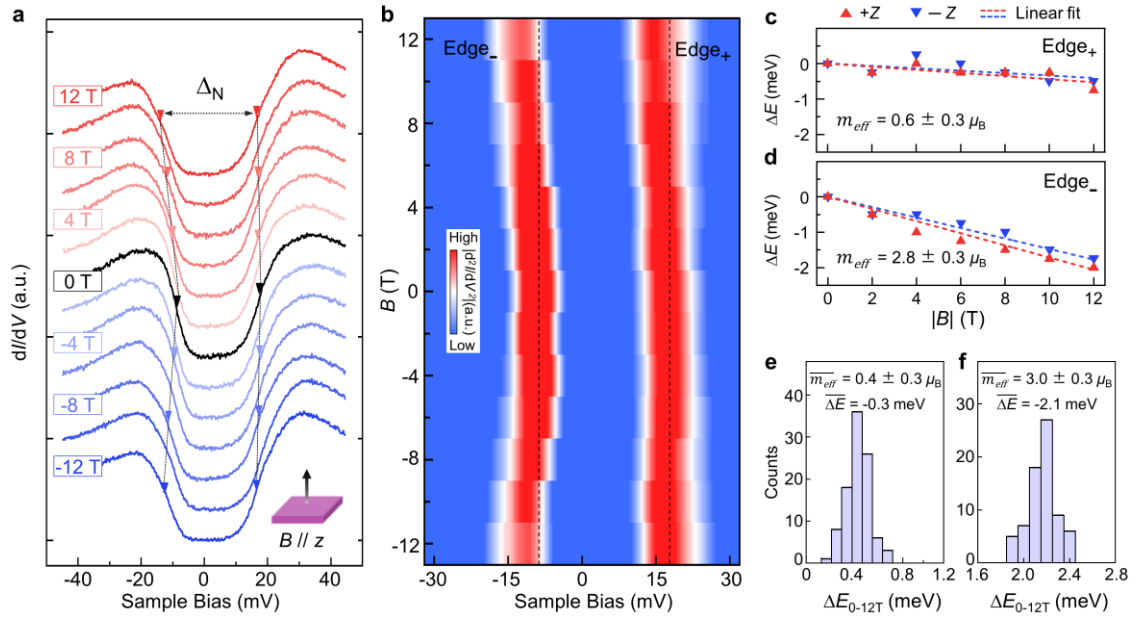


Fig. 4 | Spin polarization of the correlated insulator. **a**, Magnetic field dependence of the gap (centre site for illustration). The magnetic field is perpendicular to the sample surface and ranges from -12 T to 12 T. The Δ_N is marked by the arrows. **b**, Second derivative of the field-dependent tunnelling spectra, *i.e.*, $|d^2I/dV^2|$. The peaks in the $|d^2I/dV^2|$ spectra are the energy levels of the unoccupied/occupied edges (Edge₊/Edge₋). The black dashed lines in (b) indicate the energy locations of the peaks at $B = 0$ T. **c**, **d**, Energy shifts of Edge₊/Edge₋ as functions of the external field, respectively. The effective magnetic moment values can be derived as $m_{eff} = 0.6 \pm 0.3 \mu_B$ and $2.8 \pm 0.3 \mu_B$. Histogram of the energy shifts over the MTB superlattice, showing an average value of $0.4 \pm 0.3 \mu_B$ (e) and $3.0 \pm 0.3 \mu_B$ (f) of Edge₊/Edge₋.

Such net magnetic moments cannot be solely attributed to the magnetizations induced by an external field (*e.g.*, Pauli paramagnetism)³⁸ by considering the following facts: the B -independent moments derived from the linear energy shifts and no signature of splitting in the spectral line shapes under the magnetic field. In addition, our data show no saturation of the energy shifts to the maximum field (12 T) applied in our experiments (Figs. 4c and 4d), which is not favourable for the possibility of spin-orientation-dependent quantum phases, such as those seen in Fe_3Sn_2 ^{39,40}. Therefore, we conclude that with the formation of the MTB superlattice, monolayer $\text{MoTe}_{56/33}$ possesses spontaneous magnetizations (at least locally), and the correlated insulating state might be closely interrelated with the magnetic structure. Moreover, the moment values are greatly different between the occupied and unoccupied sides, and the moment extracted for occupied edge states ($\sim 3 \mu_B$) is significantly larger than a pure spin Zeeman effect ($1 \mu_B$). This finding suggests that the orbital movements are nonnegligible in the total magnetism of our system.

Although DFT, by coincidence, captures the spin polarized state in a local moment picture, it is insufficient to reproduce the observed insulating gap formed at the Fermi level well (see discussions in Fig. S6). In the spin-nonpolarized case (Fig. 2c), three bands (B1–B3) contribute to the P_0 states. The SOC lifts the kagome band degeneracy at the Γ point ($\Delta_{\text{SOC}} \sim 20$ meV), and the spin degeneracy at the Γ point is lifted when the spin-exchange interaction is considered ($\Delta_{\text{ex}} \sim 100$ meV). With such splittings, a pronounced energetic separation is observed between the two spin components of B1–B3 (Fig. 2e), but E_F crosses one branch of B2 and B3. A comprehensive understanding

of the magnetic properties (*e.g.*, ground states, long-range order, and gap origin) demands combinations of multiple analytical techniques, especially tuning the filling factor, and theoretical simulations beyond the local moment picture^{41,42}. This investigation will be a follow-up work because it is beyond the scope of the present work, which aims mainly to introduce a new 2D crystalline structure with FB-driven correlated physics.

In conclusion, we have established a monolayer kagome system with FB-driven correlated magnetism in the monolayer MoTe_{33/56}, which is known to be a highly controllable and scalable phase. Theoretical calculations confirm the formation of multiple kagome flat bands in the MTB superlattice. In the partially filled bands, the electron correlations lead to a gap opening as large as 15 meV. The magnetization-polarized Zeeman shifts provide strong evidence of spontaneous spin polarizations. Further studies are expected to investigate the doping dependence of the correlated insulator by tuning the carrier density. Our work presents a new strategy for designing monolayer vdW materials that manifest strong correlation effects, and it opens versatile opportunities for tailoring nontrivial emergent quantum phenomena.

Methods

Sample preparation. In this study, samples were grown on bilayer graphene formed by heating SiC (0001) in a home-built molecular beam epitaxy (MBE) system with a base pressure of $\sim 1.2 \times 10^{-10}$ Torr. Te (99.999%) was evaporated from Knudsen cells, and High-purity Mo (99.95%) was evaporated from an e-beam evaporator, respectively. The flux ratios of Mo/Te were 1:30. To obtain the ordered MTB superstructure, one follows the following procedure. The substrate was kept at ~ 250 °C during the deposition. After deposition, the sample was annealed for 10 min at the growth temperature with the Te flux maintained. Subsequently, the substrate temperature was increased to 450 °C and annealed for 1 hour (with the Te flux off).

STM/ Q-plus AFM measurements. The STM/STS measurements were performed by a commercial Unisoku 1300 system (base pressure $< 1 \times 10^{-10}$ Torr). Electrochemically etched W-tips were used in all measurements, which are calibrated spectroscopically against the Shockley surface states of cleaned Cu (111) surfaces before performing measurements on MoTe₂. STM topographic images are acquired in constant-current mode. The dI/dV spectra are measured using a standard lock-in amplifier with modulation at a frequency of 932 Hz; other parameters are specified in figure captions. All STM/S measurements were taken at 4.3 K unless otherwise specified.

The nc-AFM imaging is performed by the frequency shift (Δf) of the qPlus resonator in constant-height mode with an oscillation amplitude of 100 pm. The resonance frequency of the AFM probe is $f_0 = 29.10$ kHz, and its quality factor Q is 57962.

DFT calculation. The theoretical calculations were performed using the VASP package based on DFT. The electron-ion potential and exchange-correlation functional were described by projected augmented wave (PAW) and generalized gradient approximation (GGA)^{43,44}, respectively. For the relaxation of geometric structures, the kinetic energy cutoff is set to 350 eV. A $3\times 3\times 1$ Monkhorst Pack k-point grid was used for structure optimization, whereas a denser $7\times 7\times 1$ grid for electronic calculation⁴⁵. As a double-check, the energy cutoff was set to 500 eV and a $5\times 5\times 1$ k-mesh was used to verify the calculation results. The vacuum region of 20 Å was used to avoid the periodic interaction. The stress force and energy convergence criteria are chosen as 0.01 eV/Å and 10^{-5} eV, respectively. All atoms were allowed to be fully optimized to the ground state without considering van der Waals dispersion corrections. The band decomposed charge density was calculated by reading the converged wave-function file. The irreps calculations were performed using the IRVSP program in conjunction figurewith VASP⁴⁶.

Acknowledgements

This work was supported by the National Key R&D Program of China (Grant No. 2018YFA0703700, No. 2018YFE0202700, No. 2022YFA1402401), the National Natural Science Foundation of China (12134011, 12174291, 11974012, 11974422, and 12204534), the fellowship of China Postdoctoral Science Foundation (Grant No. 2021M702532) and the Strategic Priority Research Program of Chinese Academy of Sciences (XDB30000000). the Fundamental Research Funds for the Central

Universities, and the Research Funds of Renmin University of China [Grants No. 22XNKJ30 (W.J.) and No. 23XNH077 (J.D.)]. All numerical calculations presented in this paper were performed on the supercomputing system in the Supercomputing Center of Wuhan University.

References

1. Derzhko, O., Richter, J. & Maksymenko, M. Strongly correlated flat-band systems: the route from Heisenberg spins to Hubbard electrons. *Int. J. Mod. Phys. B* **29**, 1530007 (2015).
2. Regnault, N. et al. Catalogue of flat-band stoichiometric materials. *Nature* **603**, 824-828 (2022).
3. Bergman, D. L., Wu, C. & Balents, L. Band touching from real-space topology in frustrated hopping models. *Phys. Rev. B* **78**, 125104 (2008).
4. Wang, L. et al. Correlated electronic phases in twisted bilayer transition metal dichalcogenides. *Nat. Mater.* **19**, 861-866 (2020).
5. Abbas, G. et al. Recent advances in twisted structures of flatland materials and crafting moiré superlattices. *Adv. Funct. Mater.* **30** (36), 2000878 (2020).
6. Li, T. et al. Continuous Mott transition in semiconductor moiré superlattices. *Nature* **597**, 350-354 (2021).
7. Anderson, E. et al. Programming correlated magnetic states via gate controlled moiré geometry. Preprint at <https://arxiv.org/abs/2303.17038> (2023).
8. Cao, Y. et al. Correlated insulator behaviour at half-filling in magic-angle graphene superlattices. *Nature* **556**, 80-84 (2018).
9. Xie, M. & MacDonald, A. H. Nature of the correlated insulator states in twisted bilayer graphene. *Phys Rev Lett.* **124**, 097601 (2020).
10. Liu, X. et al. Tunable spin-polarized correlated states in twisted double bilayer graphene. *Nature* **583**, 221-225 (2020).

11. Tschirhart, C. L. et al. Imaging orbital ferromagnetism in a moiré Chern insulator. *Science* **372**, 1323-1327 (2021).
12. Cao, Y. et al. Unconventional superconductivity in magic-angle graphene superlattices. *Nature* **556**, 43-50 (2018).
13. Oh, M. et al. Evidence for unconventional superconductivity in twisted bilayer graphene. *Nature* **600**, 240-245 (2021).
14. Ye, L. et al. Massive Dirac fermions in a ferromagnetic kagome metal. *Nature* **555**, 638-642 (2018).
15. Kang, M. et al. Dirac fermions and flat bands in the ideal kagome metal FeSn. *Nat. Mater.* **19**, 163-169 (2020).
16. Yin, J.-X. et al. Negative flat band magnetism in a spin-orbit-coupled correlated kagome magnet. *Nat. Phys.* **15**, 443-448 (2019).
17. Xing, Y. et al. Localized spin-orbit polaron in magnetic Weyl semimetal $\text{Co}_3\text{Sn}_2\text{S}_2$. *Nat. Commun.* **11**, 5613 (2020).
18. Li, M. et al. Dirac cone, flat band and saddle point in kagome magnet YMn_6Sn_6 . *Nat. Commun.* **12**, 31292 (2021).
19. Huang, H. et al. Flat-band-induced anomalous anisotropic charge transport and orbital magnetism in kagome metal CoSn . *Phys Rev Lett.* **128**, 096601 (2022).
20. Sun, Z. et al. Observation of topological flat bands in the kagome semiconductor Nb_3Cl_8 . *Nano Lett.* **22**, 4596-4602 (2022).
21. Lei, L. et al. Electronic Janus lattice and kagome-like bands in coloring-triangular MoTe_2 monolayers. Preprint at <https://arxiv.org/abs/2302.06166> (2023).
22. Najmaei, S. et al. Vapour phase growth and grain boundary structure of molybdenum disulphide atomic layers. *Nat. Mater.* **12**, 754-759 (2013).
23. Liu, H. et al. Dense network of one-dimensional midgap metallic modes in monolayer MoSe_2 and their spatial undulations. *Phys Rev Lett.* **113**, 066105 (2014).
24. Zhu, T. et al. Imaging gate-tunable Tomonaga-Luttinger liquids in 1H- MoSe_2 mirror twin boundaries. *Nat. Mater.* **21**, 748-753 (2022).
25. Jolie, W. et al. Tomonaga-Luttinger liquid in a box: electrons confined within

- MoS₂ mirror-twin boundaries. *Phys. Rev. X* **9** (1), 011055 (2019).
26. Barja, S. et al. Charge density wave order in 1D mirror twin boundaries of single-layer MoSe₂. *Nat. Phys.* **12**, 751-756 (2016).
 27. Chen, J. et al. Quantum effects and phase tuning in epitaxial hexagonal and monoclinic MoTe₂ monolayers. *ACS Nano* **11**, 3282-3288 (2017).
 28. Dong, Lu, et al. Charge density wave states in 2H-MoTe₂ revealed by scanning tunneling microscopy. *Chinese. Phys. Lett.* **35**, 066801 (2018).
 29. Yu, Y. et al. Phase-controlled growth of one-dimensional Mo₆Te₆ nanowires and two-dimensional MoTe₂ ultrathin films heterostructures. *Nano Lett.* **18**, 675-681 (2018).
 30. He, X. et al. Selective self-assembly of 2,3-diaminophenazine molecules on MoSe₂ mirror twin boundaries. *Nat. Commun.* **10**, 2847 (2019).
 31. Zhu, H. et al. Defects and surface structural stability of MoTe₂ under vacuum annealing. *ACS Nano* **11**, 11005-11014 (2017).
 32. Batzill, M. Mirror twin grain boundaries in molybdenum dichalcogenides. *J. Phys. Condens. Matter* **30** (49), 493001 (2018).
 33. Bradlyn, B. et al. Topological quantum chemistry. *Nature* **547**, 298-305 (2017).
 34. Elcoro, L. et al. Double crystallographic groups and their representations on the Bilbao Crystallographic Server. *J. Appl. Crystallogr.* **50**, 1457-1477 (2017).
 35. Liu, H., Meng, S. & Liu, F. Screening two-dimensional materials with topological flat bands. *Phys. Rev. Mater.* **5** (8), 084203 (2021).
 36. Vano, V. et al. Artificial heavy fermions in a van der Waals heterostructure. *Nature* **599**, 582-586 (2021).
 37. Yang, X. et al. Possible phason-polaron effect on purely one-dimensional charge order of Mo₆Se₆ nanowires. *Phys. Rev. X* **10**, 031061 (2020).
 38. Fujita, N. et al. Direct observation of electrically induced Pauli paramagnetism in single-layer graphene using ESR spectroscopy. *Sci. Rep.* **6**, 34966 (2016).
 39. Yin, J. X. et al. Giant and anisotropic many-body spin-orbit tunability in a strongly correlated kagome magnet. *Nature* **562**, 91-95 (2018).

40. Ren, Z. et al. Plethora of tunable Weyl fermions in kagome magnet Fe_3Sn_2 thin films. *npj Quantum Mater* **7** (1), 109 (2022).
41. Jung, J., Zhang, F. & MacDonald, A. H. Lattice theory of pseudospin ferromagnetism in bilayer graphene: competing interaction-induced quantum Hall states. *Phys. Rev. B* **83**, 115408 (2011).
42. Bultinck, N., Chatterjee, S. & Zaletel, M. P. Mechanism for anomalous Hall ferromagnetism in twisted bilayer graphene. *Phys. Rev. Lett.* **124**, 166601 (2020).
43. Perdew, J. P., Burke, K. & Ernzerhof, M. Generalized gradient approximation made simple. *Phys. Rev. Lett.* **78**, 1396-1396 (1997).
44. Blöchl, P. E. Projector augmented-wave method. *Phys. Rev. B* **50**, 17953-17979 (1994).
45. Monkhorst, H. J. & Pack, J. D. Special points for Brillouin-zone integrations. *Phys. Rev. B* **13**, 5188-5192 (1976).
46. Gao, J., Wu, Q., Persson, C. & Wang, Z. Irvsp: To obtain irreducible representations of electronic states in the VASP. *Comput. Phys. Commun.* **261**, 107760 (2021).